*lubricants*

*Article*

# Evolution of the Geometric Structure of X39Cr13 Steel upon Thermochemical Treatment Specific to Medical-Grade Steels

**Monika Gwoździk [1,*], Mirosław Bramowicz [2] and Sławomir Kulesza [2]**

[1] Faculty of Production Engineering and Materials Technology, Czestochowa University of Technology, 42-201 Czestochowa, Poland
[2] Faculty of Technical Sciences, University of Warmia and Mazury in Olsztyn, Oczapowskiego 11, 10-719 Olsztyn, Poland; mbramowicz@moskit.uwm.edu.pl (M.B.); kulesza@matman.uwm.edu.pl (S.K.)
* Correspondence: monika.gwozdzik@pcz.pl

**Abstract:** This paper presents the results of the multi-aspect surface characterization of X39Cr13 steel samples subjected to technological processes specific to medical instrumentation, such as heat and thermochemical treatment, as well as sterilization, which are implemented in corrosion resistance measurements. The application of numerical methods of fractal analysis to averaged profiles obtained from SEM images resulted in double-log plots of structure function, from which the determination of the fractal parameters of interest was possible. The discussion was focused on the fractal dimension D, which governs relative height variations upon scaling in length, and corner frequency $f_c$, which separates the scaling behavior of different-order structures (particles and their aggregates). The obtained results show that the heat treatment leaves behind a granular structure of steel ($D_2$ = 2.43; $f_{c2}$ = 1.97 nm), whereas corrosion tests reveal the appearance of pits ($D_1$ = 2.17; $f_{c1}$ = 0.303 nm; $D_2$ = 2.59; $f_{c2}$ = 4.76 nm). In turn, the ion nitriding improves the resistance of steel X39Cr13 to local corrosion. The fractal analysis also shows that the structure of the nitrided layer differs insignificantly from that of the untreated material, seen only as a shortening of the radius of the self-similarity area by a factor of two ($f_{c2}$ = 1 nm).

**Keywords:** fractal analysis; X39Cr13 steel; SEM

check for updates

**Citation:** Gwoździk, M.; Bramowicz, M.; Kulesza, S. Evolution of the Geometric Structure of X39Cr13 Steel upon Thermochemical Treatment Specific to Medical-Grade Steels. *Lubricants* **2022**, *10*, 114. https://doi.org/10.3390/lubricants10060114

Received: 7 April 2022
Accepted: 1 June 2022
Published: 3 June 2022



## 1. Introduction

Surface topography is an important characteristic that helps us to understand the wide range of chemical and biological processes occurring at the point of contact between biomaterials and the tissue environment. Surface geometry is the most frequently used parameter for testing the surface layer of biomaterials. For example, the adhesion of bacteria increases with increased roughness. Some spatial details, such as geometry or symmetry, are important for determining the adherence of bacteria [1]. Surface modifications are used to obtain the appropriate surface geometry. The authors of [2] modified the surface of 316 L steel using low-voltage micro-arc oxidation in order to produce porous layers, the chemical composition of which depends on the chemical composition of the parent material and the electrolyte used. It has been shown that the surface topography of the porous layer is dependent on the voltage increase. In addition, the oxides and layers formed are very tightly packed, which hinders the diffusion of Fe ions, thus protecting them from further oxidation and contributing to an increase in corrosion resistance. The created porous layer is a specific barrier that prevents the penetration of environmental factors into the implant core as well as the diffusion of alloying elements into the tissues surrounding the implant. Similarly, the aim of the study [3] was to analyze the effect of laser irradiation on zirconium implants in order to enhance the topographic aspects of the surface and the biological response to osseointegration. When testing materials used in biomaterials, corrosion resistance is as important as surface topography. The corrosion resistance of these materials can be tested in reagents that simulate body fluids, such as a simulated bovine serum [4], artificial saliva [5], Ringer solution [6], or Tyrode solution [7]. Nitriding is one of the methods related to the production of surface layers used in surface engineering to improve the properties of the surface [8,9]. Shukla et al. [10] showed a five-fold increase in hardness after nitriding. In turn, Kartikasari et al. [11] attempted to increase the corrosion resistance of the Fe-10Al-25Mn alloy by means of plasma nitriding, which was considered to be one of the most cost-effective surface treatments. The authors of [12] focus on the comparison of three plasma nitriding variants: (I) DC plasma nitriding, (II) active screen plasma nitriding, and (III) an active screening process with bias voltage application. The research was extended by studying the coverage of the active screen. A mixture of two gases, $N_2$–$H_2$, was applied during nitriding. An unalloyed steel, C45E, was used as the substrate. The researchers showed that layer thickness and surface hardness were higher when using active, screen-biased plasma nitriding with a high $N_2$ content gas mixture. The use of active screening did not have a significant impact on the chemical composition of the layer. On the other hand, Zhu et al. [13] studied the influence of prefabricated Cu–Ti foil on the macrostructure and mechanical properties of a multiphase coat obtained by the means of plasma nitriding. The layer was applied to the C17200 Cu alloy. The authors have shown that, to a large extent, the composition of a multiphase coat, obtained as a result of plasma nitriding, depends on the ratio of Cu/Ti atoms in the prefabricated Cu–Ti gradient layers. It was shown that small amounts of Ti–N compounds, as well as specific Cu–Ti inter-metals, formed in three types of Cu–Ti film. In turn, when the authors of [14] applied atmospheric pressure using thermal nitrogen plasma, the AlN-strengthening layer was prepared on 1060 and 6082 substrates. The microstructures of these nitrided layers may be divided into three areas: the area of lamellae that exists at the top, a dendritic region beneath it, and a transition area situated beneath both. Furthermore, researchers have shown that molten Al moves upwards via voids and capillaries in AlN structures. In addition, it was found that, by increasing the intensity of $N_2$ flow from 1 L/min to 7.5 L/min, the properties of the nitrided layers, such as their hardness and wear resistance, will improve. Moreover, the nitrided layer becomes thicker. Tao et al. [15] studied an austenitic iron–nickel alloy, Invar (R) 36 and RA 330 (R). This alloy was subjected to a treatment consisting of triode plasma nitriding (TPN). The process was carried out at a temperature of 400–450 °C. The researchers revealed that nitrogen-induced lattice expansion occurs below the nitride-containing surface layer in Invar 36 alloy after TPN treatment, implying that Cr is not necessary for the nitrogen-interstitial-induced lattice expansion phenomenon to occur also suggesting another type of gamma (N). More and more studies related to nitriding focus on nitriding corrosion-resistant steels [16–21]. Lin et al. [16] studied plasma-nitrided austenitic stainless steel. The authors showed that, by controlling the surface characteristics of austenitic stainless steel, the blood-compatible quality of plasma nitriding improved the anticoagulant properties, making austenitic stainless steels suitable candidates in the field of surgical and medical instruments. Steel X39Cr13 is classified as martensitic steel [22,23]. This steel is widely used as a biomedical material. Because of its good mechanical properties and high corrosion resistance in the environment of physiological liquids, it is used in the production of surgical instruments [23,24]. The durability of elements used in surgery, apart from the use of an appropriate material in terms of its chemical composition and structure, has a large impact on the surface topography of a given element. Because of this, fractal analysis is being used more and more often to study the surface topography of biomaterials [25,26]. The fractal dimension is a valuable parameter with which to determine surface roughness [27,28] and study bio-adhesion [29].

Studies related to the application of scanning electron microscopy (SEM) [30] and atomic force microscopy (AFM) [25,31] are of great importance, especially in fractal analysis. The authors of [25] studied the three-dimensional surface micromorphology of zinc/silver-particle-composite antibacterial coatings. The surface was prepared using an electrodeposition technique. The measurements showed that a 3D topographic fractal parameter contributed significantly to the estimation of the 3D surface micromorphology of Zn/AgPs. This surface directly or indirectly influenced the physical and antibacterial properties. The authors showed that the distribution of height values and fractal geometry-based parameters have the potential to be used as tools to quantify and identify different 3D geometrical patterns in composite coatings such as Zn/AgPs. In turn, the authors of [32] showed the relationships between the tensile properties and fractal dimensions of the fracture surfaces of Ti-6Al-4V alloy using SEM stereoscopy coupled with 3D measurements. It was observed that the fractal dimension was proportional to the roughness of the fracture surface. Both the yield strength and ultimate tensile strength decreased, while ductility increased with the increase in fractal dimension due to the change in the fracture mode, depending on the microstructure induced by the heat treatment.

This study concerns the structural characterization of engineering biomaterial and aims to reveal a correlation between the fractal parameters determined from SEM images and the method of formation and functional features of the surface layer. The main aim of this paper was to find a link between the functional features of the surface layer of medical-grade stainless steel and methods and its thermochemical treatment using fractal parameters as scale-invariant measures of surface height variations. The fractal parameters determined from SEM images can reveal the stereometric characteristics of the outer surface layer obtained technologically.

## 2. Materials and Methods

The material under study comprised steel specimens containing 0.42 wt.% C, 13.73 wt.% Cr, 0.55 wt.% Mn, and 0.39 wt.% Si. This steel is classified as stainless-steel grade X39Cr13 according to the standard EN [33]. Tests were carried out on 1-mm-thick specimens. X39Cr13 steel samples were hardened and tempered, then subjected to further treatments. The heat treatment consisted of quenching at an austenitizing temperature of 1050 °C. The time for which this temperature was maintained was 20 min. After quenching, the steel was subject to two hours of tempering at 300 °C. Heating and austenitizing, as well as tempering, were carried out in a vacuum furnace with compressed nitrogen cooling (marking H + T). After the heat treatment, some of the samples were subjected to additional nitriding (marking H + T + N) performed in a glow-discharge vacuum chamber (nitriding furnace). The samples in the chamber were connected to a cathode, while the furnace housing served as the anode. The nitriding was carried out at T = 460 °C and pressure $p$ = 145 Pa for time $t$ = 20 h. The reactive atmosphere contained 25% molecular nitrogen diluted with molecular hydrogen. During glow discharge, gases were dissociated, excited, and ionized. Then, a sterilization process was carried out on some of the samples, both heat-treated (marked H + T + S) and surface-treated (marked H + T + N + S).

Sterilization by steam was carried out in an autoclave at T = 134 °C with pressure $p$ = 0.21 MPa for t = 0.5 h in four cycles. Finally, corrosion resistance tests were applied to the following samples: heat-treated (marked H + T + C); heat-treated and sterilized (marked H + T + S + C); heat-treated and nitrided (marked H + T + N + C); and heat-treated, nitrided, and sterilized (marked H + T + N + S + C).

Corrosion resistance tests were performed in Tyrode's physiological solution (pH = 6.8 ÷ 7.4). Deionized water with a resistivity of 18.2 MΩcm was used to prepare a physiological solution. Prior to electrochemical treatment, the samples were degreased in acetone and rinsed in an ultrasonic bath. Figure 1 presents a detailed diagram of the processes performed.

The surface was observed by means of a Jeol JSM-6610LV scanning electron microscope. Based on the data obtained from SEM, fractal analysis of the studied surfaces was carried out.

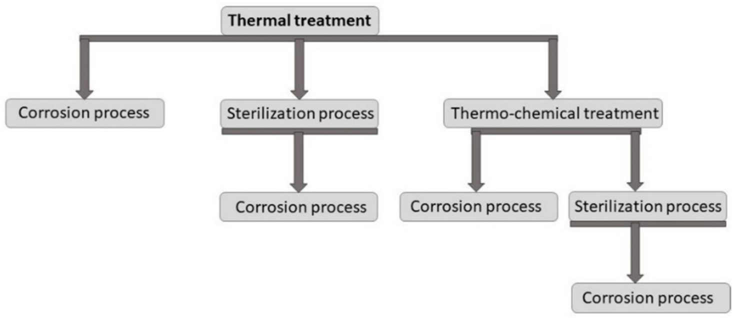


**Figure 1.** Process tree showing the sequences of the thermochemical treatment procedures.

## 3. Results and Discussion

SEM images (shown in Figures 2–10, as an example) were used to determine the scale-invariant characteristics of the surface patterning of the samples under investigation. Note, however, that digitized SEM images provide pixels with intensity in the greyscale associated with the number of locally scattered electrons rather than the surface height. However, allometric characterization also works without the proper scaling of vertical dimensions; hence, unitless pixel intensities could have been taken for a relative quasi-height-data series.

To this end, the original SEM images were first row-wise averaged to obtain the mean height profile function, $z_{av}(x)$ (example shown in Figure 11), which was processed to obtain the structure function according to the following Formula (1):

$$S(r) = \frac{1}{(N-m)} \sum_{p=1}^{N-m} \left(z_{av}(p) - z_{av}(r)\right)^2 \tag{1}$$

where $p$ addresses the height samples in the mean profile and r defines the shift between the input data and their lagged duplicate. Phenomenologically, Thomas et al. demonstrated that any one-dimensional structure function can be approximated using independent parameters related to the surface patterning [34] Equation (2):

$$S(r) = 2S_q^2\left[1 - \exp\left(-\left(\frac{r}{\xi}\right)^{2\alpha}\right)\right] \tag{2}$$

where $S_q$ is the long-range rms surface roughness, $\alpha$ is the Hurst exponent, and $\xi$ is the horizontal correlation length. Note that, for the lengths much longer than $\xi$, the exponential term vanishes and the plot saturates at $2S_q{}^2$. On the other hand, in the limit $r << \xi$, Equation (2), reduced to its first-order Taylor expansion components, turns into $A \cdot r^{2\alpha}$, where A is constant. Therefore, the mean profile of the structure function depends allometrically on the length $\tau$, related to the fractal character of surface height variations (3):

$$S_{av}(\tau) = K\tau^{2(2-D)} \tag{3}$$

where $D$ is the scale-invariant fractal dimension and $K$ is the amplitude scaling factor. In general, $D$ controls the relative amplitude of surface roughness, whereas $K$ controls the absolute amplitude of surface roughness at different length scales. Allometric scaling results in a constant slope on a double-log plot of a structure function associated with the fractal dimension, which ends at a threshold of $f_c$, referred to as the corner frequency (example shown in Figure 12). Sharp variations in the slope are specific to multifractal surfaces with high-order aggregates.

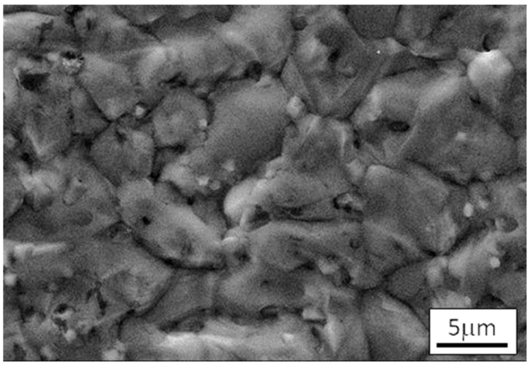


**Figure 2.** SEM, steel after hardening and tempering.

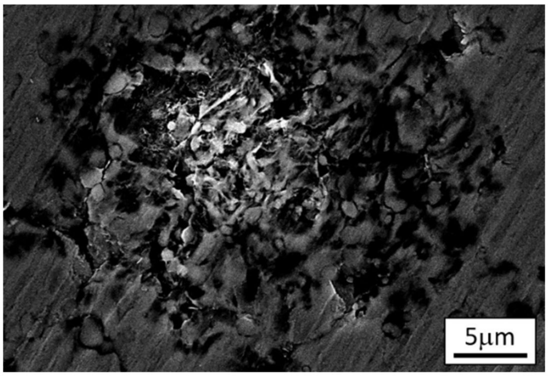


**Figure 3.** SEM, steel after heat treatment and test corrosion with exemplary pitting.

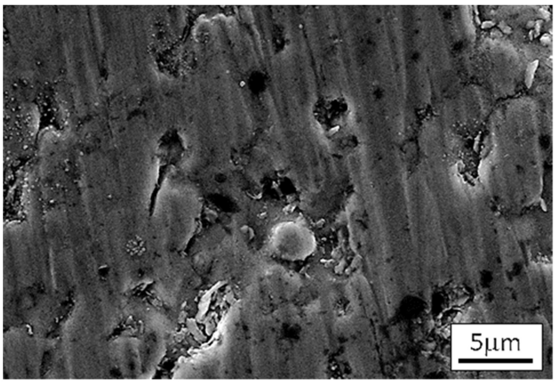


**Figure 4.** SEM, steel after heat treatment and sterilization.

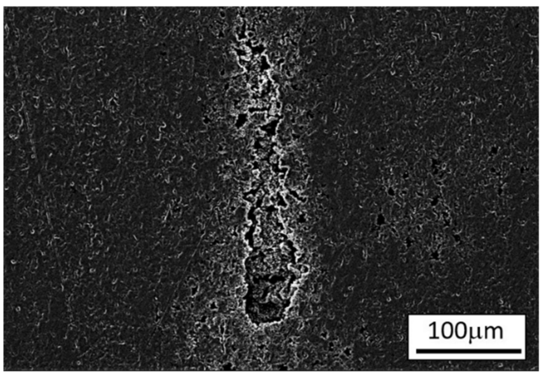


**Figure 5.** SEM, steel after heat treatment, sterilization, and test corrosion.

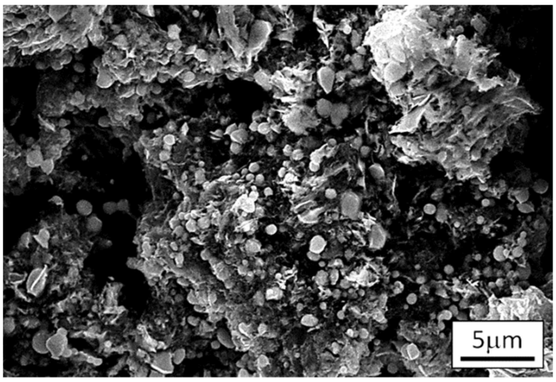


**Figure 6.** SEM, steel after heat treatment, sterilization, and test corrosion with exemplary pitting.

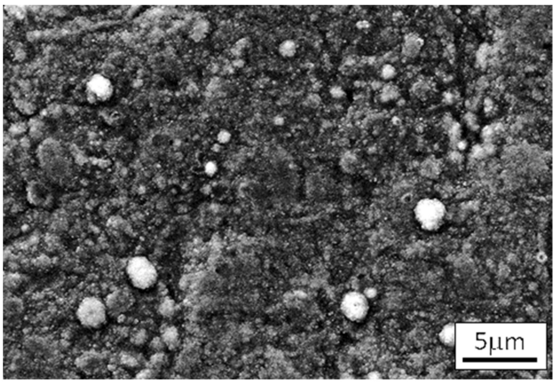


**Figure 7.** SEM, steel after heat treatment and thermochemical treatment.

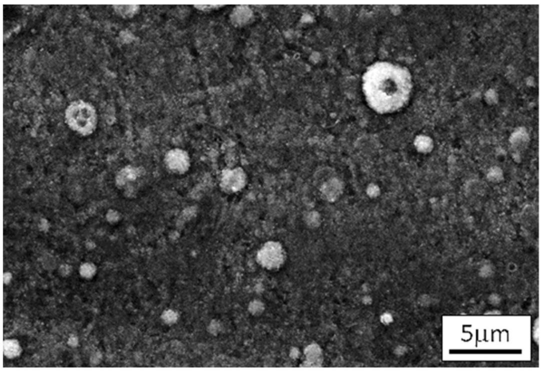


**Figure 8.** SEM, steel after heat treatment, thermochemical treatment, and test corrosion.

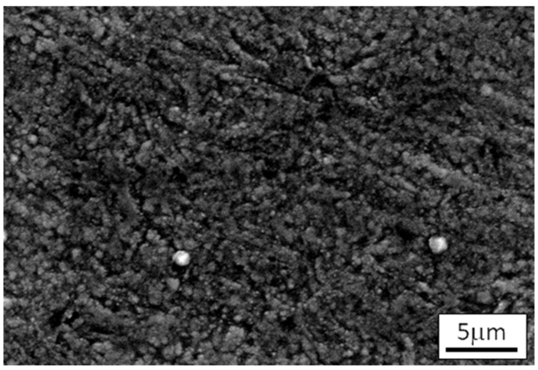


**Figure 9.** SEM, steel after heat treatment, thermochemical treatment, and sterilization.

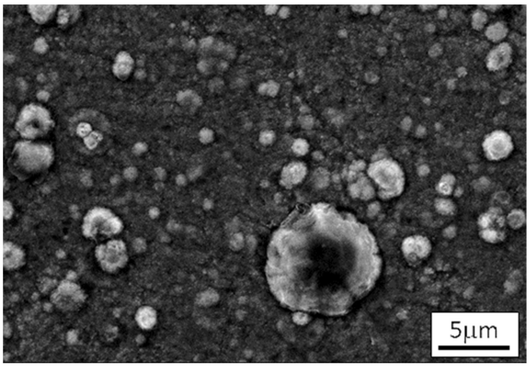


**Figure 10.** SEM, steel after heat treatment, thermochemical treatment, sterilization, and test corrosion.

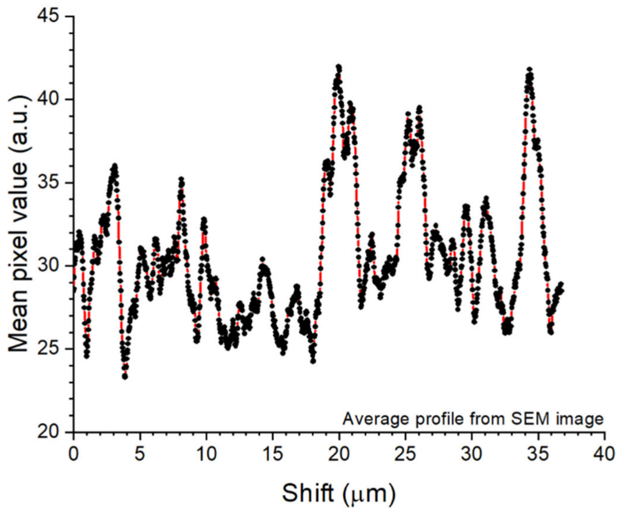


**Figure 11.** Example digital processing of SEM image of X39Cr13 steel sample towards fractal parameters—mean profile of the SEM image.

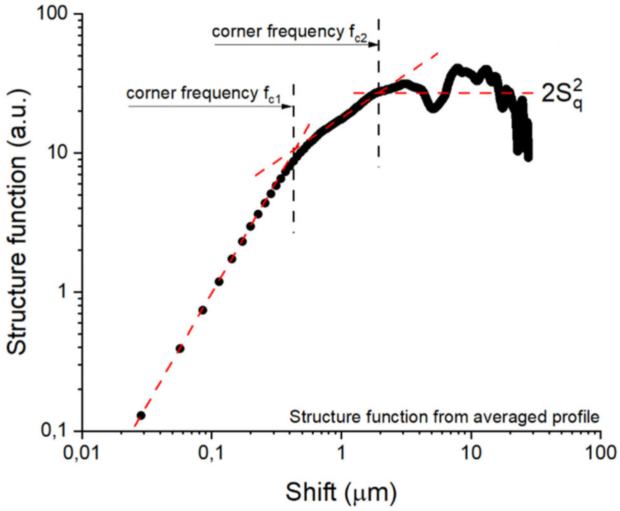


**Figure 12.** Example digital processing of the SEM image of X39Cr13 steel sample towards fractal parameters—double-log plot of the structure function computed from the mean profile, demonstrating the method of estimation of fractal dimension D and corner frequency $f_c$, which separates the scaling behaviors of structures of various orders (particles and their aggregates).

Table 1 presents the results of fractal analysis for averaged profiles of SEM images originating from samples of steel X39Cr13 at various stages of thermochemical treatment.

**Table 1.** Fractal descriptors of the surface topography derived from row-wise-averaged profiles of SEM images of X39Cr13 steel samples: $D_1$, $D_2$—unitless fractal dimensions; $f_{c1}$, $f_{c2}$—corner frequencies.

| Process | $D_1$ [-] | $f_{c1}$ [nm] | $D_2$ [-] | $f_{c2}$ [nm] |
|---|---|---|---|---|
| H + T | - | - | 2.43 | 1.97 |
| H + T + C (inside of the pit) | 2.17 | 0.303 | 2.59 | 4.76 |
| H + T + C (outside of the pit) | - | - | 2.50 | 1.58 |
| H + T + S | - | - | 2.41 | 1.71 |
| H + T + S + C (inside of the pit) | 2.18 | 0.292 | 2.44 | 2.88 |
| H + T + S + C (outside of the pit) | - | - | 2.39 | 1.27 |
| H + T + N | - | - | 2.39 | 1.00 |
| H + T + N + C | - | - | 2.46 | 1.25 |
| H + T + N + S | 2.32 | 0.216 | 2.76 | 5.99 |
| H + T + N + S + C | 2.20 | 0.430 | 2.65 | 1.93 |

The obtained results demonstrate a monofractal and moderately developed (D = 2.43) structure for the top layer of the studied X39Cr13 steel after quenching and tempering at T = 300 °C (Figure 2). The average range of self-similar behavior (set by the corner frequency $f_c$ and related to the size of the dominant elements of the structure) does not exceed 2 μm, which is approximately 70 scanning steps. Previous works on this steel have reported its tempered martensite structure with prevailing precipitates of $M_3C$ carbides [35]. Studies related to fractal analyses carried out on steel X39Cr13 have shown that the results strongly depend on the processes performed [36–38]. For example, fractal analyses carried out on steel X39Cr13, quenched only, have shown [36] that small carbide precipitates occur randomly over the entire surface of the sample. However, they are most frequently situated close to grain boundaries. On this surface, carbides are revealed as light areas. On the other hand, studies carried out on annealed steel have characterized the surface as rough, with carbide precipitates hundreds of nanometers in size being seen [38]. While the surface of quenched and high-temperature-tempered (T = 620 °C) steel X39Cr13 is rough, with small, sharp, eagle-like precipitates (mainly $M_{23}C_6$ [35]), these precipitates show a luminous color in the light of electrons [37]. Further testing of the corrosion resistance (Figure 3) resulted in the appearance of a small number of pits. The inner surface structure of these pits was found to be bifractal, being a mixture of primarily fine-grained structures aligned to form long-range secondary agglomerates. The former contributes to a poorly developed surface (D = 2.17) range of approximately 0.30 μm (around 10 pixels), while the latter is clearly more developed (D = 2.59) and embraces places separated by no more than 4.80 μm from each other. In contrast, the structure of the nearby areas remains monofractal, similar to that of the first stage (D = 2.50, $f_c$ = 1.58 μm). Furthermore, in previous works by the authors [38], after the corrosion test, the annealed steel featured the presence of regular pits a few hundred micrometers in diameter and an aspect ratio of around two. These pits had a granular nature. In the next step, the heat-treated sample was sterilized. A comparison of the obtained fractal characteristics proves that this process also has negligible effects on the structure of the steel (Figure 4). However, after a subsequent corrosion resistance test (Figures 5 and 6), pits appeared on the surface similar to those seen in Figure 3. As noted previously, the inner structure of the pits was found to be bifractal, with smooth fine-shaped grains (D = 2.18, $f_c$ = 0.29 μm) grouped in rough clusters (D = 2.59) in a slightly shorter range ($f_c$ = 2.88 μm). Likewise, the outer structure of nearby areas remained monofractal and nearly identical to that of the initial stage (D = 2.39, $f_c$ = 1.27 μm). According to the authors of [39], the corrosion potential ($E_{kor}$) for such processes increases over time and stabilizes at a level of −0.08 ÷ −0.05 V. These two processes are favorable to surface oxidation and passivation. As a result, quenching and low-temperature tempering are found to retard the process of general corrosion in

Tyrode's liquid. In addition, for these processes, sudden rushes of current were observed on polarization curves within the range of potentials 0.1 ÷ 0.3 V. Such a course proves the nucleation of pits and the development of local corrosion on this type of material. In this case, the chlorine ion is responsible for the pitting; its concentration in the Tyrode's solution is roughly 0.15 M. Figures in the literature show that both austenitization parameters during quenching [40] and tempering parameters [41], which, in martensitic steel, must ensure the required anti-corrosion and mechanical properties, are equally important. The mechanical properties of steels containing 0.45% carbon and 13% chromium strongly depend on the austenitization temperature, and for any improvement in that aspect, the carbides present in the steel need to dissolve in austenite [40]. The presence of undissolved primary carbides has a negative impact on the properties of this steel. In turn, an increase in the tempering temperature results in a lowering of mechanical properties, such as the yield strength and tensile strength [40]. According to Arntz et al. [41], a tempering temperature of <480 °C ensures good resistance to general corrosion because, subsequently, tempered martensite with (Fe, Cr)$_3$C carbide precipitates exists in the structure. Another heat-treated sample was subjected to surface nitriding (Figure 7). It was found that the structure of the top layer changed only in terms of having a smaller radius of self-similarity area ($f_c$ = 1 µm). Both the fractal dimension (D = 2.39) and the multiplicity of fractal characteristics were found to be intact after nitriding. However, Figure 8 shows that this process significantly increases the corrosion resistance of the studied steel due to its unchanged surface structure (D = 2.46, $f_c$ = 1.25 µm). Despite this, deeper in the subsurface layer of the nitrided steel, some processes that are responsible for the arrangement of a complex cluster structure must occur, as revealed after subsequent sterilization (Figure 9). Unlike previously seen clusters, Table 1 details the fine- and coarse-grained phases with much more developed surfaces (fractal dimensions 2.32 and 2.76, respectively); at the same time, the cluster size is three times larger than in the initial layer (Figure 2)—6 µm vs. 2 µm, respectively. The heat-treated steel contains moderately isotropic structures, while the nitrided steel may be classified as strongly isotropic. Apart from that, all of the surfaces show monofractal features, which were mostly affected by the presence of spherical grains. Fractal dimensions lie in a narrow range specific to well-developed surfaces. Moreover, allometric invariance disappears shortly after reaching a limit of a few hundred nanometers, as determined by the corner frequency. In this case, the corner frequency was found to correlate with the size of the spherical grains, which suggests that geometrical structures closely correspond to scale-independent measures. Studies have shown that ion nitriding accelerates the transpassivation of steel and results in the disappearance of secondary passivity [39]. Shukla et al. [10] showed that nitrided alloy displays increased corrosion resistance in comparison to untreated alloy. The method of substrate preparation does not only affect the fractal analysis. The assumptions of Tillmann et al. [42] consisted of obtaining very important information related not only to microstructural properties but also to the tribomechanical properties of nitride coats: TiAlN and CrAlN. These coats were deposited on steel AISI H11 prepared according to three variants: (1) the nitriding of the annealed substrate, (2) the quenching and double tempering of the steel, and (3) nitridation subsequent to a heat treatment of the substrate. The method of magnetron spraying was used to produce the coats. The prepared substrate was found to have a great influence on the microstructure, adhesion, and wear resistance of the TiAlN coat. Instead, in the case of the CrAlN coat, the substrate preparation was found to have no significant impact on its properties. Heat and surface treatments are techniques generally proven to be useful for improving mechanical properties by causing changes to the surface of materials [18]. In summary, steel X39Cr13 is a popular, medical-grade material used for various instruments, including surgical ones [23]. Such steel can replace ferritic and austenitic corrosion-resistant steels. Apart from heat treatment, this steel may be subjected to surface treatment, e.g., ion nitriding, because such a treatment is more frequently applied to alloy steels, which are also subjected to passivation. Plasma nitriding allows for surface activation in alloy steels with a passive layer. The combination of heat and surface treatments enables better practical properties to be obtained for medical instruments made of X39Cr13 steel. The process of sterilization is used in practice not only as a disinfection treatment but also to ensure relaxation in own stresses, e.g., after sharpening or operating.

## 4. Conclusions

Based on the microstructure investigations and fractal analyses, the following statements and conclusions can be formulated:

1. The structure of the top layer of the initial steel (after quenching and tempering) is monofractal (granular) ($D_2$ = 2.43; $f_{c2}$ = 1.97 nm).
2. Corrosion tests performed on heat-treated steels show their heterogeneous surfaces composed of bifractal, clustered pits (a mixture of fine- and coarse-grained structures of various alignment lengths) next to an unchanged structure outside the pits ($D_1$ = 2.17; $f_{c1}$ = 0.303 nm; $D_2$ = 2,59; $f_{c2}$ = 4.76 nm).
3. Nitriding substantially strengthens corrosion resistance and slightly modifies the structure of the top layer of steel: it shortens the range of the self-similarity area (granularity) without changing their degree of development and multiplicity of description ($f_{c2}$ = 1 nm).
4. Temperature was found to be the main factor influencing the properties of the layer generated on the examined steel.
5. Fractal characteristics were found to be reliable measures of surface development as well as reliable descriptors of the spatial structure of the surface layer. These characteristics allowed us to recognize the effects of surface degradation.

**Author Contributions:** Conceptualization, M.G.; methodology, M.G., M.B. and S.K.; formal analysis, M.G., M.B. and S.K.; investigation, M.G., M.B. and S.K.; software, M.G., M.B. and S.K.; writing—original draft preparation, M.G., M.B. and S.K.; writing—review and editing, M.G. All authors have read and agreed to the published version of the manuscript.

**Funding:** This research received no external funding.

**Institutional Review Board Statement:** Not applicable.

**Informed Consent Statement:** Not applicable.

**Data Availability Statement:** The data presented in this study are available on request from the authors.

**Conflicts of Interest:** The authors declare no conflict of interest.

## References

1. Holban, A.M.; Farcasiu, C.; Andrei, O.C.; Grumezescu, A.M.; Farcasiu, A.T. Surface modification to modulate microbial biofilms-applications in dental medicine. *Materials* **2021**, *14*, 6994. [CrossRef]
2. Ossowska, A.; Ryl, J.; Sternicki, T. Production and properties of the porous layer obtained by the electrochemical method on the surface of austenitic steel. *Materials* **2022**, *15*, 949. [CrossRef]
3. Cunha, W.; Carvalho, O.; Henriques, B.; Silva, F.S.; Ozcan, M.; Souza, J.C.M. Surface modification of zirconia dental implants by laser texturing. *Lasers Med. Sci.* **2022**, *37*, 77–93. [CrossRef]
4. Geringer, J.; Fridrici, V.; Ding, H.H.; Kim, K.; Taylor, T.; Semetse, L.; Ehsani-Majd, S.; Olubambi, P.; Fontaine, J.; Kapsa, P. Some hard or soft coatings to protect the pristine biometallic substrates under fretting-corrosion solicitations: What should be the best solution? *Lubricants* **2020**, *8*, 55. [CrossRef]
5. Hussein, M.A.; Kumar, A.M.; Abdelaal, A.F.; Azeem, M.A. Surface analysis and in vitro corrosion properties in artificial saliva of surface-treated Ti6Al4V alloy for dental applications. *Metall. Mater. Trans. A Phys. Metall. Mater. Sci.* **2021**, *52*, 4299–4309. [CrossRef]
6. Garcia-Falcon, C.M.; Gil-Lopez, T.; Verdu-Vazquez, A.; Mirza-Rosca, J.C. Corrosion behavior in Ringer solution of several commercially used metal alloys. *Anti-Corros. Methods Mater.* **2021**, *68*, 324–330. [CrossRef]
7. Bo, W.; Chenghao, L.A.; Peng, W. Electrochemical characteristics of the hydroxyapatite coatings prepared by Mg sacrificial anode. *Rare Met. Mater. Eng.* **2010**, *39*, 2069–2074. [CrossRef]
8. Li, X.Y.; Dou, W.B.; Tian, L.H.; Dong, H.S. Combating the tribo-corrosion of LDX2404 lean duplex stainless steel by low temperature plasma nitriding. *Lubricants* **2018**, *6*, 93. [CrossRef]
9. Ramos, H.E.L.; Franco, A.R., Jr.; Vieira, E.A. Influence of plasma nitriding pressure on microabrasive wear resistance of a microalloyed steel. *J. Mater. Res. Technol.* **2019**, *8*, 1694–1700. [CrossRef]

10. Shukla, K.; Sugumaran, A.A.; Khan, I.; Ehiasarian, A.P.; Hovsepian, P.E. Low pressure plasma nitrided CoCrMo alloy utilising HIPIMS discharge for biomedical applications. *J. Mech. Behav. Biomed. Mater.* **2020**, *111*, 104004. [CrossRef]
11. Kartikasari, R.; Effendy, M. Surface characterization of Fe-10Al-25Mn alloy for biomaterial applications. *J. Mater. Res. Technol.* **2021**, *15*, 409–415. [CrossRef]
12. Kovacs, D.; Quintana, I.; Dobranszky, J. Effects of different variants of plasma nitriding on the properties of the nitrided layer. *J. Mater. Eng. Perform.* **2019**, *28*, 5485–5493. [CrossRef]
13. Zhu, Y.D.; Yan, M.F.; Zhang, Q.L.; Wang, Q.W.; Zhuo, H.Y. Effects of the prefabricated Cu-Ti film on the microstructure and mechanical properties of the multiphase coating by thermo plasma nitriding on C17200 Cu alloy. *Coatings* **2019**, *9*, 694. [CrossRef]
14. Li, X.; Xin, W.D.; Zheng, X.Y.; Ren, Z.A.; Sun, D.Q.; Lu, W.L. Microstructural characterization and formation mechanism of nitrided layers on aluminum substrates by thermal plasma nitriding. *Metals* **2019**, *9*, 523. [CrossRef]
15. Tao, X.; Matthews, A.; Leyland, A. On the nitrogen-induced lattice expansion of a non-stainless austenitic steel, Invar 36 (R), under triode plasma nitriding. *Metall. Mater. Trans. A Phys. Metall. Mater. Sci.* **2020**, *51*, 436–447. [CrossRef]
16. Lin, Y.H.; Lan, W.C.; Ou, K.L.; Liu, C.M.; Peng, P.W. Hemocompatibility evaluation of plasma-nitrided austenitic stainless steels at low temperature. *Surf. Coat. Technol.* **2012**, *206*, 4785–4790. [CrossRef]
17. Chong, S.O.; Kim, S.J. Effects of plasma jon nitriding temperatures on cavitation-erosion resistance of STS 304 in seawater. *Acta Phys. Pol. A* **2019**, *135*, 968–971. [CrossRef]
18. Mateescu, A.O.; Mateescu, G.; Balan, A.; Ceaus, C.; Stamatin, I.; Cristea, D.; Samoila, C.; Ursutiu, D. Stainless steel surface nitriding in open atmosphere cold plasma: Improved mechanical, corrosion and wear resistance properties. *Prime Arch. Mater. Sci.* **2021**, *14*, 4836. [CrossRef]
19. Dalibon, E.L.; Czerwiec, T.; Trava-Airoldi, V.J.; Ghafoor, N.; Rogstrom, L.; Oden, M.; Bruhl, S.P. Characterization of DLC coatings over nitrided stainless steel with and without nitriding pre-treatment using annealing cycles. *J. Mater. Res. Technol.* **2019**, *8*, 1653–1662. [CrossRef]
20. De Araujo Junior, E.; Bandeira, R.M.; Manfrinato, M.D.; Moreto, J.A.; Borges, R.; Vales, S.D.; Suzuki, P.A.; Rossino, L.S. Effect of ionic plasma nitriding process on the corrosion and micro-abrasive wear behavior of AISI 316L austenitic and AISI 470 super-ferritic stainless steels. *J. Mater. Res. Technol.* **2019**, *8*, 2180–2191. [CrossRef]
21. Aizawa, T.; Yoshino, T.; Morikaw, K.; Yoshihar, S.I. Microstructure of plasma nitrided AISI420 martensitic stainless steel at 673 K. *Crystals* **2019**, *9*, 60. [CrossRef]
22. Fischer, B.; Neidel, A. Intergranular corrosion in retaining rings made of X39CrMo17-1 and X39Cr13. *Prakt. Metallogr.* **2014**, *51*, 463–474. [CrossRef]
23. Gilewicz, A.; Chmielewska, P.; Murzynski, D.; Dobruchowska, E.; Warcholinski, B. Corrosion resistance of CrN and CrCN/CrN coatings deposited using cathodic arc evaporation in Ringer's and Hank's solutions. *Surf. Coat. Technol.* **2016**, *299*, 7–14. [CrossRef]
24. López, R.; Menéndez, M.; Fernández, C.; Chmiela, A.; Bernardo-Sánchez, A. The influence of carbon coatings on the functional properties of X39Cr13 and 316LVM steels intended for biomedical applications. *Metals* **2019**, *9*, 815. [CrossRef]
25. Méndez, A.; Reyes, Y.; Trejo, G.; Stępień, K.; Ţălu, Ş. Micromorphological characterization of zinc/silver particle composite coatings. *Microsc. Res. Tech.* **2015**, *78*, 1082–1089. [CrossRef]
26. Moldovan, M.; Prodan, D.; Popescu, V.; Prejmerean, C.; Saroşi, C.; Saplonţai, M.; Ţălu, Ş.; Vasile, E. Structural and morphological properties of HA-ZnO powders prepared for biomaterials. *Open Chem.* **2015**, *13*, 725–733. [CrossRef]
27. Salehi, M.; Noordermeer, J.W.M.; Reuvekamp, L.A.E.M.; Blume, A. Characterization of counter-surface substrates for a laboratory abrasion tester (LAT100) compared with asphalt and concrete to predict car tire performance. *Lubricants* **2022**, *10*, 8. [CrossRef]
28. Violano, G.; Afferrante, L. Roughness-induced adhesive hysteresis in self-affine fractal surfaces. *Lubricants* **2021**, *9*, 7. [CrossRef]
29. Pimienta, C.; Dubuc, B.; Tawashi, R. Surface fractal dimension and the quantification of roughness of titanium implant material. *Cells Mater.* **1994**, *4*, 379–386.
30. Sinha, S.D.; Das, S.; Tarafdar, S.; Dutta, T. Monitoring of wild pseudomonas biofilm strain conditions using statistical characterization of scanning electron microscopy images. *Ind. Eng. Chem. Res.* **2017**, *56*, 9496–9512. [CrossRef]
31. Anu, A.; Khadar, M.A. Grain size tuning of nanostructured $Cu_2O$ films through vapour phase supersaturation control and their characterization for practical applications. *AIP Adv.* **2015**, *5*, 097176. [CrossRef]
32. Venkatesh, B.; Chen, D.L.; Bhole, S.D. Three-dimensional fractal analysis of fracture surfaces in a titanium alloy for biomedical applications. *Scr. Mater.* **2008**, *59*, 391–394. [CrossRef]
33. *EN 10088-1*; Stainless Steels—Part 1: List of Stainless Steels. European Committee for Standardization: Brussels, Belgium; p. 1995.
34. Thomas, R.R.; Rosén, B.G.; Amini, N. Fractal characterization of the anisotropy of rough surfaces. *Wear* **1999**, *232*, 41–50. [CrossRef]
35. Gwoździk, M. Optymization of heat and surface treatment of X39Cr13 steel designated for surgical instruments. In *Collective Monograph: Material and Exploitation Problems in Modern Materials Engineering*; Monograph No.2; Faculty of Processes and Materials Engineering and Applied Physics: Czestochowa, Poland, 2009; pp. 73–93, ISBN 978-83-8745-23-3.
36. Gwoździk, M.; Kulesza, S.; Bramowicz, M.; Bałaga, Z. Surface morphology analysis of martensitic stainless steel after different treatments. *Acta Phys. Pol.* **2019**, *135*, 157–161. [CrossRef]
37. Gwoździk, M.; Kulesza, S.; Bramowicz, M. Surface morphology analysis of X39Cr13 steel using for biomedical application. In Proceedings of the 28th International Conference on Metallurgy and Materials (METAL 2019), Brno, Czech Republic, 22–24 May 2019; pp. 1022–1027.

38. Gwoździk, M.; Bramowicz, M.; Kulesza, S. Application of fractal geometry methods for analysis of X39Cr13 steel after heat and surface treatments. In Proceedings of the 27th International Conference on Metallurgy and Materials (METAL 2018), Brno, Czech Republic, 23–25 May 2018; pp. 1114–1120.
39. Gwoździk, M.; Nitkiewicz, Z.; Bala, H.; Tokarz, A. The influence of various heat and surface treatments on the corrosion resistance of martensitic steel in a physiological environment. *Inżynieria Materiałowa* **2010**, *176*, 984–986. (In Polish)
40. De Anders, C.G.; Caruana, G.; Alvares, L.F. Control of $M_{23}C_6$ carbides in 0.45C-13Cr martensitic stainless steel by means of three representative heat treatment parameters. *Mater. Sci. Eng.* **1998**, *A241*, 211–215. [CrossRef]
41. Heimanne, W.; Oppenheime, R.; Wessling, W. Stainless Steels. In *Steel: A Handbook for Materials Research and Engineering, Volume 2: Application*; Eisenhüttenleute, V.D., Ed.; Springer: Berlin/Heidelberg, Germany, 1993; Chapter C13; pp. 382–422.
42. Tillmann, W.; Grisales, D.; Stangier, D.; Butzke, T. Tribomechanical behaviour of TiAlN and CrAlN coatings deposited onto AISI H11 with different pre-treatments. *Coatings* **2019**, *9*, 519. [CrossRef]